

UNIVERSITY OF ZARAGOZA

Faculty of Science

Final Master's Project

**Metal-coordinated molecular networks on  
Cu(111) surfaces: from structure to magnetism**

September 2017

*Author:*

Leyre Hernández López

*Supervisors:*

Jorge Lobo Checa

Fernando Bartolomé Usieto



# Content

ABSTRACT .....	1
1. INTRODUCTION .....	1
2. METHODS AND MATERIALS .....	2
2.1. Scanning Tunnelling Microscopy .....	2
2.1.1. Tunnel effect .....	2
2.1.2. STM set up and working principles .....	4
2.2. Low Energy Electron Diffraction (LEED) .....	6
2.3. Sample preparation under ultra-high vacuum conditions .....	6
2.3.1 Cu(111) substrate preparation .....	7
2.3.2 Molecular evaporation.....	7
2.3.3 Metal evaporation.....	9
3. RESULTS .....	10
3.1. Molecular networks .....	10
3.1.2 Porous phase.....	10
3.1.2 Close packed phase .....	13
3.2. Network modification upon transition metal evaporation .....	15
3.2.1 Manganese interaction with DCA networks. ....	15
3.2.2 Cobalt interaction with DCA networks .....	17
3.2.3 Iron interaction with DCA networks.....	21
4. CONCLUSIONS .....	27
5. BIBLIOGRAPHY .....	29
6. APPENDICES .....	31
Appendix 1: LEED .....	31
Appendix 2: Porous network LEED pattern .....	33
Appendix 3: Profile heights of Co clusters .....	34
Appendix 4: Images Fe on pristine Cu(111).....	36

## **ABSTRACT**

This work focuses on the growth and characterization of three different transition metals (Mn, Fe and Co) upon selected molecular networks under ultra-high vacuum conditions. The resulting self-assembled structures are characterized by means of Scanning Tunnelling Microscopy and Low Energy Electron Diffraction. We use a Cu(111) monocrystal as substrate and generate two well-characterized and extended molecular networks that are partially covered or disrupted by the addition of the transition metals. From the highly resolved STM images we can study their mutual interaction and we detect structures that vary from regular nanodots to one dimensional chains.

## **1. INTRODUCTION**

Scanning Probe Microscopies are used to study the condensed matter at the atomic scale. They consist of a probe (tip) which is in close proximity, but generally not in contact, to a surface in order to measure their mutual interaction. With the invention of scanning probe techniques and the availability of ultra-high vacuum environments, it is now possible to develop and explore Surface Science fields. This Final Master Project reports the nano-scale modification that transition metals can induce onto a self-assembled molecular network, by means of scanning tunnelling microscopy (STM) as the main experimental tool.

One of the objectives of this work was to learn how to grow structures "in-situ" and to become familiar with the STM operation and its corresponding data acquisition and analysis. Scientifically, the aim was firstly to form a two dimensional supramolecular network using a molecular precursor (9,10-dicyanoanthracene molecules) onto a Cu(111) surface. Once formed, we studied the modification induced upon the presence of three transition metals (Fe, Co and Mn).

In this memory, we show that metal coordinated molecular networks exhibit periodical, long range order on the surface. When transition metals are deposited onto it, they induce different kinds of interactions and reveal a tendency to destroy the network, lifting up molecules or changing its arrangement. Moreover, we observe that the molecular coordination can change drastically with the presence of the transition metals (for example, cobalt deposited on copper coordinates with two molecules instead of three, as copper does).

## 2. METHODS AND MATERIALS

### 2.1. Scanning Tunnelling Microscopy

The scanning tunnelling microscope (STM) was invented in 1981 by Gerd Binnig and Heinrich Rohrer, who demonstrated its capability to image metal surfaces with unprecedented atomic resolution<sup>1,2</sup>. Since then, it has become a powerful tool in the field of Surface Science, allowing the analysis of the outer crust of conductive materials in real space with lateral and vertical resolution. The basic set-up consists of an atomically sharp metallic tip that is closely approached ( $\sim 10^{-9}$  m) to the surface of a conducting or semi-conducting sample. When a bias voltage is applied at such nanometric distances between these two electrodes, a tunnelling current is produced. This current stems from a quantum mechanical process and depends exponentially on the tip-sample distance, giving rise to highly sensitive surface measurements.<sup>3</sup>

#### 2.1.1. Tunnel effect

The tunnel effect is the basic principle of the STM. It takes place between states separated by a finite potential barrier, such as conductor-insulator-conductor systems. Classically, a particle having less energy than the potential barrier cannot go through it. However, quantum mechanics states that if this potential barrier is thin and low enough, a light particle (such as an electron) has a significant probability to make it across, i.e. tunnel through<sup>4</sup>. In this case, the tip and the sample constitute the conductive materials and the vacuum gap between them is the potential barrier (see Fig. 1).

There are several approaches to model the tunnel effect<sup>3</sup>. One of them was proposed by Bardeen<sup>5</sup>, who considered tip and sample as independent systems and included the tunnelling Hamiltonian as a perturbation. By applying the Fermi's golden rule, the tunnelling current can be expressed as:

$$I = \frac{4\pi e}{\hbar} \int_{-\infty}^{\infty} [f_t(E_F + E - eV_{bias}) - f_s(E_F + E)] \rho_t(E_F + E - eV_{bias}) \rho_s(E_F + E) |M(E_F + E - eV_{bias}, E_F + E)|^2 dE \quad (\text{Eq. 1})$$

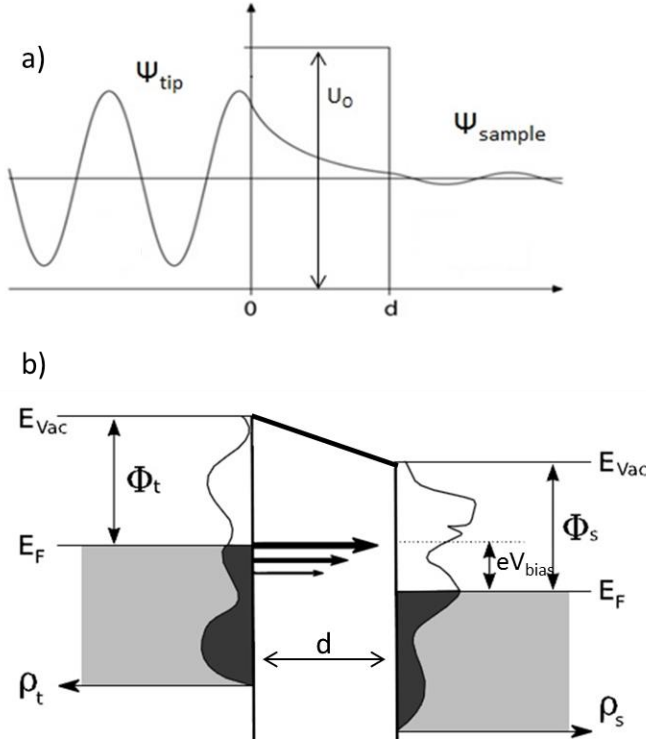


**Figure 1.** a) Potential barrier of energy  $U_0$  and width  $d$  and the wavefunctions of a particle tunnelling from left to right. Image adapted from ref<sup>6</sup>. b) Density of states of tip and sample for an applied voltage  $U$ . Fermi levels are shifted with respect to one another and a current appears that will be proportional to the density of states of the sample (and tip). Image adapted from ref<sup>7</sup>.

where  $M$  is the tunnelling matrix,  $f_{t/s}$  are the Fermi-Dirac distributions for tip and sample respectively,  $\rho_{t/s}$  their corresponding density of states,  $E_F$  the Fermi energy and  $V_{bias}$  the bias voltage. For low temperatures,  $f_t(E_F + E - eV_{bias})$  and  $f_s(E_F + E)$  can be approximated as step functions and  $M$  can be considered constant, so the tunnelling current at a constant distance  $d$ , can be expressed as:

$$I \propto \int_0^{eV} \rho_t(E + E_F) \rho_s(E + E_F - eV_{bias}) dE \quad (\text{Eq. 2})$$

Eq. 2 depends essentially on the density of states of tip and sample and on the applied voltage. Later on, Tersoff and Hamman formulated another approach where the tip was considered metallic, ending in spherical s- electronic states<sup>8</sup>. In that way, the contribution of the tip to the current is essentially constant, and the current becomes proportional to the local density of states (LDOS) of the sample. The tunnelling current depends also on the applied  $V_{bias}$  and has an exponential dependence on the tip-sample distance. The value of the voltage gives access to the different electronic states of the studied surface. Namely, if the sample is grounded, a negative  $V_{bias}$  applied to the tip will make the tunnelling current sensitive to the unoccupied states of the system, while positive  $V_{bias}$  will probe the occupied ones.

This model holds as long as the tip does not atomically change its configuration and maintains its metallic spherical s-like termination. When this does not occur, the density of states of the tip is modified, affecting the overall tip-sample electronic states overlap and thus changing the surface topographic visualization.

### **2.1.2. STM set up and working principles**

The measurements presented in this work have been performed in a commercial Omicron low temperature STM setup shown in Figure 2. It mainly consists of two ultra-high vacuum (UHV) chambers separated by a valve: the preparation chamber and the analysis or STM chamber. A fast-entry (or load-lock) chamber, that allows a fast introduction of samples from atmospheric conditions, completes the setup. The vacuum vessels are always isolated and independently pumped except while transferring samples. The preparation chamber is equipped to perform sputtering, annealing, evaporation of molecules and metallic atoms, and characterizing the surface by means of low energy electron diffraction (LEED). It has a base pressure in the  $10^{-10}$  mbar range, whereas the STM chamber, which contains the STM stage and is used to characterise atomically the sample, has a base pressure in the low  $10^{-11}$  range.

The STM stage (tip + sample) is placed within two cryostat baths: the outer one is filled with liquid nitrogen (77K) and the inner one with liquid helium so that temperatures of 4.7 K can be reached on the tip and sample stage. Such low temperatures are important to reduce the mobility of adsorbates on the substrate that facilitates the data acquisition, while reducing the noise. In addition, possible vibrations of atoms in the sample are greatly reduced, increasing significantly the resolution in the images. Since the current exhibits an exponential dependence on the tip-sample distance, this can be used to map the surface by scanning the tip over it, i.e. recording the current point by point. Importantly, the images obtained will provide information on the electronic overlap from the surface elements and tip, but not necessarily on their atomic nuclei topography.

To acquire an image, the tip is rastered parallel to the surface plane (x, y) by means of two orthogonal piezoelectric drivers with picometer precision. There is an additional piezoelectric driver in the vertical (z) direction, which controls the tip - sample distance is operated through a feedback loop to regulate the tunnelling current. Such picometer precision demands an exceptional mechanical stability of the whole setup in order to

isolate the STM stage from external vibrations. This is achieved by introducing damping mechanisms in its design in order to decouple it from the rest of the chamber.

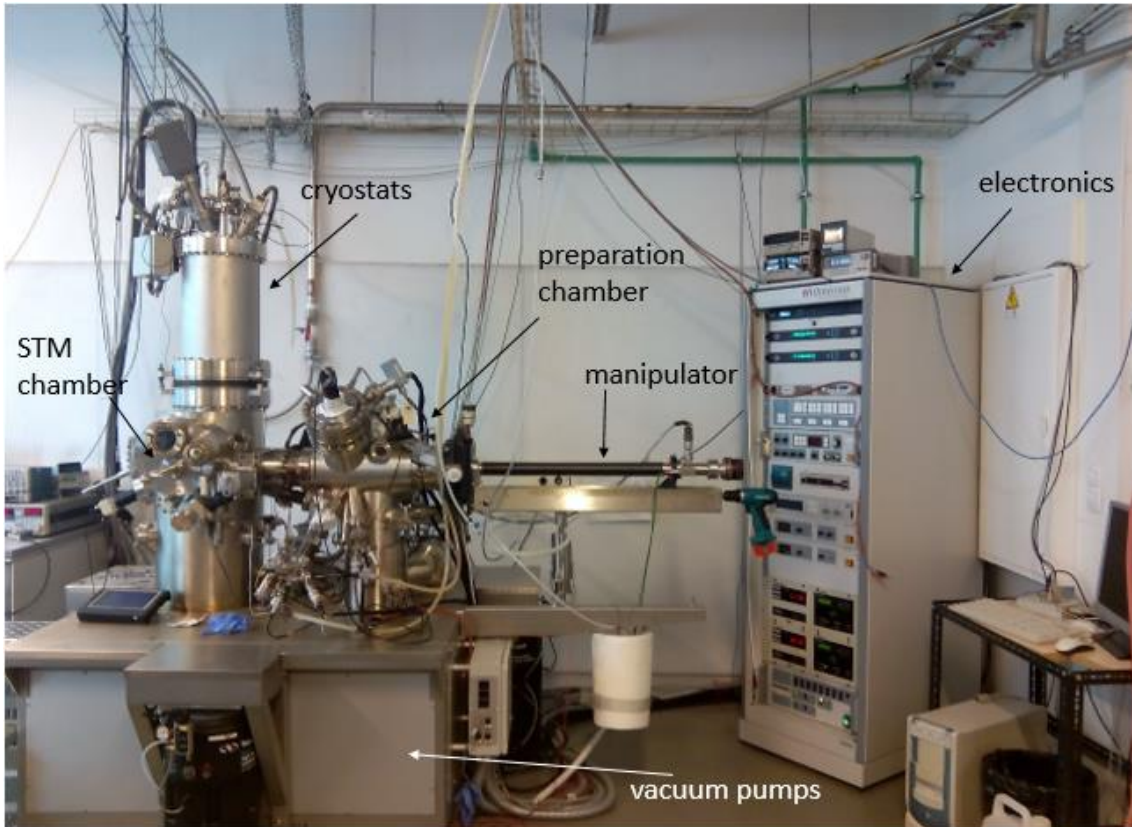


**Figure 2.** UHV system layout. There are two main parts in the experimental system: the analysis or STM chamber with the cryostats, and the preparation chamber equipped with different sputter guns, evaporators and a LEED system. The manipulator is used to move the sample between chambers. The pressure in the different chambers and main control parameters in the preparation is performed with the electronic modules piled on the rack at the side of the UHV system.

There are two different modes of imaging with STM: constant height mode or constant current mode. In the constant height mode, the tip-sample distance is maintained through the measurement, while current is recorded. At constant current, the tunnelling current is fixed and controlled through a feedback loop while changing the tip height, which is the recorded parameter (see Fig. 3). This last mode is the most generally used because it prevents crashing the tip whenever significant corrugation is present on the surface. In

particular, all the images here presented have been acquired in such constant current mode.

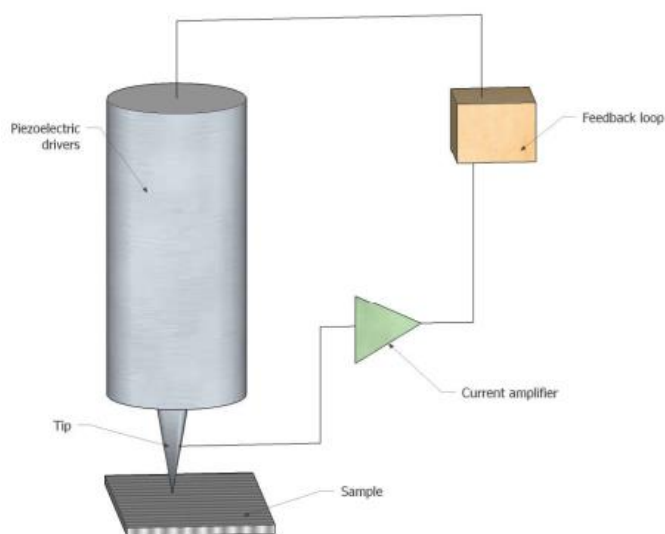


**Figure 3.** *Scheme of an STM. In constant current mode, the tunnelling current between tip and sample is measured and amplified, and the feedback loop regulates the vertical piezoelectric driver to keep this current constant.*

## 2.2. Low Energy Electron Diffraction (LEED)

Low energy electron diffraction (LEED) is a technique to analyse the periodic structures present at the surface. It consists of a collimated beam of electrons that are accelerated through the sample. They are elastically scattered following the Bragg's law and form directly the reciprocal lattice when colliding in a fluorescent screen. For further information, read Appendix 1.

## 2.3. Sample preparation under ultra-high vacuum conditions

To achieve and maintain atomically clean samples, an ultra-high vacuum environment is required. The vacuum is generated by a set of pumps operating in different pressure ranges. Rotary pumps work in the range from ambient pressure down to  $10^{-3}$  mbar. They are connected to turbo-molecular pumps that work in the range of  $10^{-1}$  mbar to  $10^{-10}$  mbar. These are complemented by ionic pumps that operate in the range of  $10^{-3}$  mbar to  $10^{-11}$  mbar. These are formed by two parallel plates that act as cathode and hollow cylinders between them with their axis perpendicular to the plates, acting as anodes. Between the plates, a magnetic field is activated, ionizing passing by molecules which are trapped within the cylinders. Finally, titanium sublimation pumps, consisting of titanium filaments, are periodically fired to improve the vacuum, as they actively pump hydrogen and other reactive species.

The pressure is measured in each chamber by means of ion gauges, consisting of a high voltage excited cylindrical grid, that ionizes the gas molecules within the vessel. These ionized molecules generate a current that is measured and correlated to the gas pressure.

### **2.3.1 Cu(111) substrate preparation**

The substrate used for our experiments was a copper monocrystal, which has a face centred cubic (fcc) structure, and terminates at the surface in a (111) plane. To achieve an atomically clean surface, repeated cycles of noble gas ion sputtering and a subsequent annealing were performed. In our case, we used argon gas for sputtering, filling the preparation chamber up to  $4 \cdot 10^{-6}$  mbar. The ions for bombardment were accelerated up to 1.1 - 1.5 kV, yielding sputtering currents of 15 - 25  $\mu$ A. The bombardment process removes any material at the surface but also strongly roughens the surface. For this reason, after sputtering, the sample must be healed by annealing it. A resistive heat assembly is available in the manipulator that allowed us to anneal up to 450°C for around 10 minutes. At this temperature, the Ar ions embedded are removed and the substrate atoms gain enough mobility to reorder into large, flat terraces that present monoatomic height steps.

### **2.3.2 Molecular evaporation**

The molecules deposited on the Cu(111) surface to generate the metal organic coordination network (MOCN) studied in this work were 9,10-dicyanoanthracene (DCA). This molecule consists of an anthracene backbone (three overlapping benzene rings) and two cyano ligands (C-N group) at the middle, as shown in figure 6. The electrostatic charge of the cyano group forms a dipole oriented from the N to the C atom, that extract negative charge from its surrounding. When these molecules are deposited onto the surface, they will lie with the anthracene backbone parallel to the Cu surface due to the interaction between the extended  $\pi$ -orbitals with the metal surface electrons<sup>9,10</sup>. In order to evaporate DCA molecules, these were sublimated from a crucible using a resistive wire at an estimated temperature of 100°C. In this process, we observed a slight increase of pressure in the chamber. Two different ordered phases were observed depending on the molecular coverage up to the monolayer (ML): a porous phase (Figure 7a) or a close packed phase (Figure 7b). In the porous network, three molecules surround each Cu adatom by coordinating through their cyano groups generating nanocavities at the

anthracene edges. On the other hand, in the close packed network, coordination atoms cannot be observed, even when the voids in the assembly suggest that they can only be stabilized by Cu adatom presence.

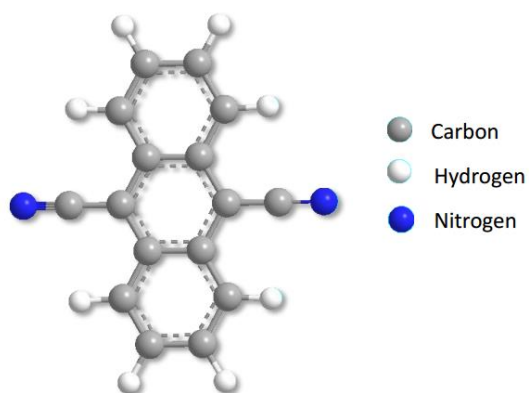


**Figure 4.** 9,10-dicyanoanthracene (DCA) molecule used for the generation of the metal-organic coordinated network.

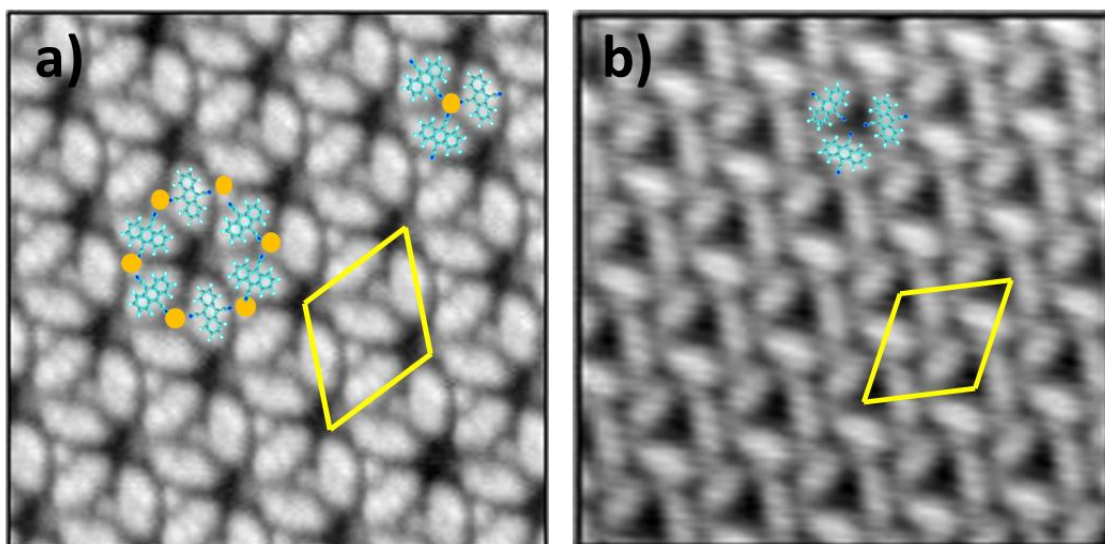


**Figure 5.** Ordered phases observed up to the full monolayer coverage. a) Porous phase. In this phase, molecules are arranged in such a way that a Cu adatom (in orange) coordinates with three cyano groups from three DCA molecules and groups of six molecules are surrounding a pore. Unitary vector size=2.15nm. STM scan details:  $I_t=300$  pA;  $V_{bias}=-1$  V; size=9x9nm<sup>2</sup>. b) Close packed phase (more densely packed). In this phase, the arrangements of three molecules are also observed without a definite pore structure and covering the whole surface. Unitary vector size=1.85nm. STM scan details:  $I_t=120$  pA;  $V_{bias}=-1$  V; size=9x9nm<sup>2</sup>.

### **2.3.3 Metal evaporation**

The metal atoms have been evaporated using a commercial electron beam evaporator. A current driven external filament emits electrons that are accelerated to the evaporating material, which is kept at high voltage, and therefore heated to substantial temperatures that sublime the material. Ions are generated in this process, which are used to monitor the overall flux, that is used as control parameter for the amount of evaporated material.

We used three different materials to investigate their interaction with the porous network. In particular, these were manganese, iron and cobalt and the formed structures will be shown in the next section.

The protocol followed for sample preparation, unless otherwise specified, has been to prepare the Cu surface (by one or two sputter-anneal cycles), formation of the porous network (after molecular evaporation), and deposition of the metallic atoms. The resulting structures have been thoroughly investigated by means of STM topographic images at 4.7 K and will be discussed in detail in the following.

## 3. RESULTS

### 3.1 Molecular networks

Supramolecular structures are usually formed due to dipole-dipole or hydrogen bonding interactions between molecules with specific functional groups<sup>11</sup>. Cyano-functionalized molecules are also able to undergo metal-organic interactions, where a metal atom or cluster acts as a node for a number of molecules<sup>12</sup>. This type of bondings are non-covalent, and allow the bond formation and breaking necessary for self-assembly processes. On the other hand, this interaction is stronger than the purely intermolecular ones, making these self-assembled structures more stable. The metal centres needed to perform metal-organic interactions can be co-deposited with the molecules or can be supplied by the metallic substrate above a certain temperature<sup>13</sup>.

The evaporation of DCA molecules on a Cu(111) substrate at room temperature gives rise to two different phases up to the monolayer, as previously described and shown in Figs. 5a and 5b. At this substrate temperature, the Cu substrate supplies enough adatoms that act as metal centres in order to form the network. As these molecules are adsorbed onto the Cu(111) substrate, they assemble into the porous phase until they completely cover the metal surface. At this point, if we continue evaporating molecules, instead of forming a second layer, the molecules will be further accommodated onto the metal. Thus, a lateral pressure is generated disrupting the porous assembly into a more compact phase (Fig. 5b). Figure 6 shows such situation, where both phases are observed to coexist.

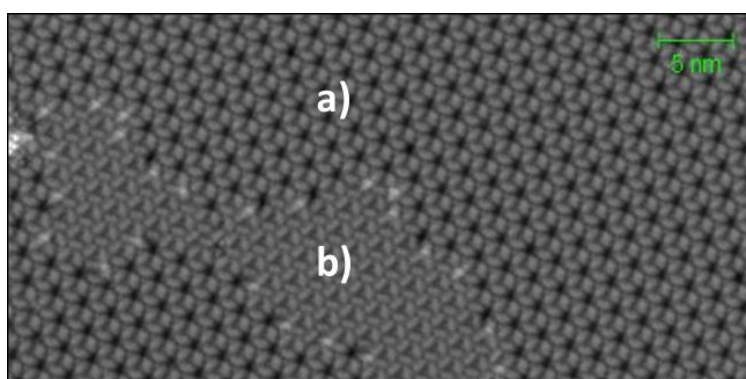


**Figure 6.** *Molecular structures below 1 ML: coexistence of a)porous and b)close packed phases. STM image at  $I_t= 300$  pA;  $V_{bias}=-1.5$  V. Size= $100 \times 50$  nm<sup>2</sup>.*

#### 3.1.2 Porous phase

The porous phase can be obtained in two ways: The first one is depositing a multilayer of molecules (there is no need to precisely control the molecular amount) and then remove the excess by annealing the substrate up to 130°C. This method has been preferentially

used in this work to obtain an extended porous network. The second method is just to evaporate a lower amount of molecules so that a fraction of the surface remains uncovered. The coverage has to be low enough to avoid the close packed phase formation (as Fig.6 shows). This method has been preferentially used in this work to obtain isolated porous islands.

When seeking extended porous networks fully covering the surface (Fig. 7 a and b), the annealing temperature is the key factor. Its calibration can be done by following the evolution of the LEED image after each sequential increase of the temperature, until the characteristic pattern of the porous network, which is a 8x8 pattern, is observed. For 22eV the LEED consists of two concentric hexagons, as shown in Fig.7c. Unfortunately, the sample temperature reading from the manipulator turned out to be inaccurate due to small variations in thermal contact after transferring samples, so it became necessary to check the LEED pattern after sample preparation. Otherwise, we might obtain the porous network in islands or a mixture of compact and porous phases.

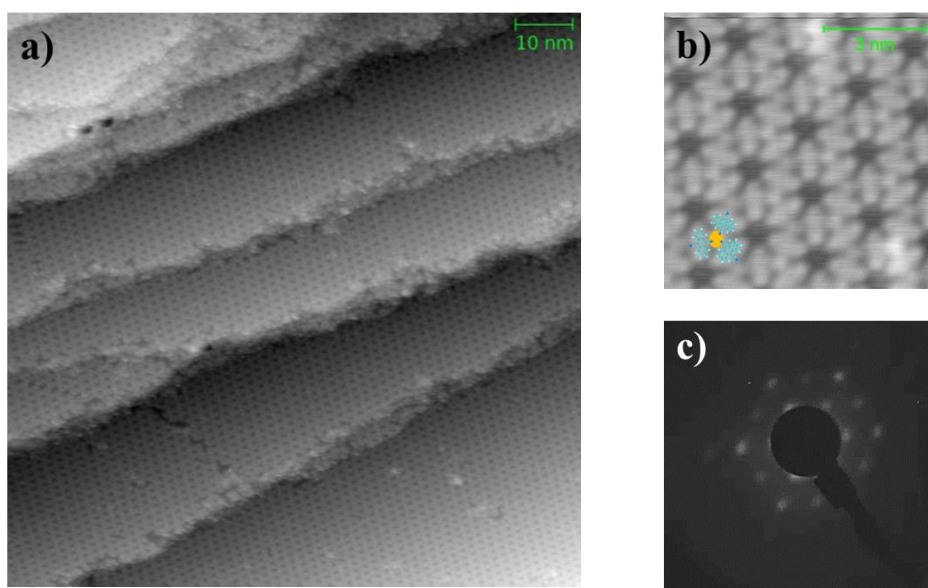


**Figure 7.** Full surface coverage of molecular porous network. a) STM image of the molecular network extending over different steps of the Cu(111) substrate.  $I_t=100\text{pA}$ ;  $V_{bias}=0.4\text{V}$ . Size= $100\times 100\text{nm}^2$  b) Close up of the network, where the darkest contrast defines the pore region.  $I_t=100\text{pA}$ ;  $V_{bias}=1.5\text{V}$ . Size= $7.5\times 7.5\text{nm}^2$ . c) LEED pattern of the porous phase: (8x8) structure. Electron beam energy is 22eV.

A correct preparation of the extended networks results in monodomain structures (that follow the crystal symmetry) and highly extended molecular networks that fill out even the smallest terraces delimited by neighbouring steps (Fig.7a). A close up of the network

is shown in Figure 7b. Here the Cu adatoms, the molecules, and the pores (darkest) can be unambiguously observed. Note that each adatom coordinates with three DCA molecules to generate the network, giving rise to an 8x8 LEED structure (Fig. 7c). For further information, see Appendix 2.

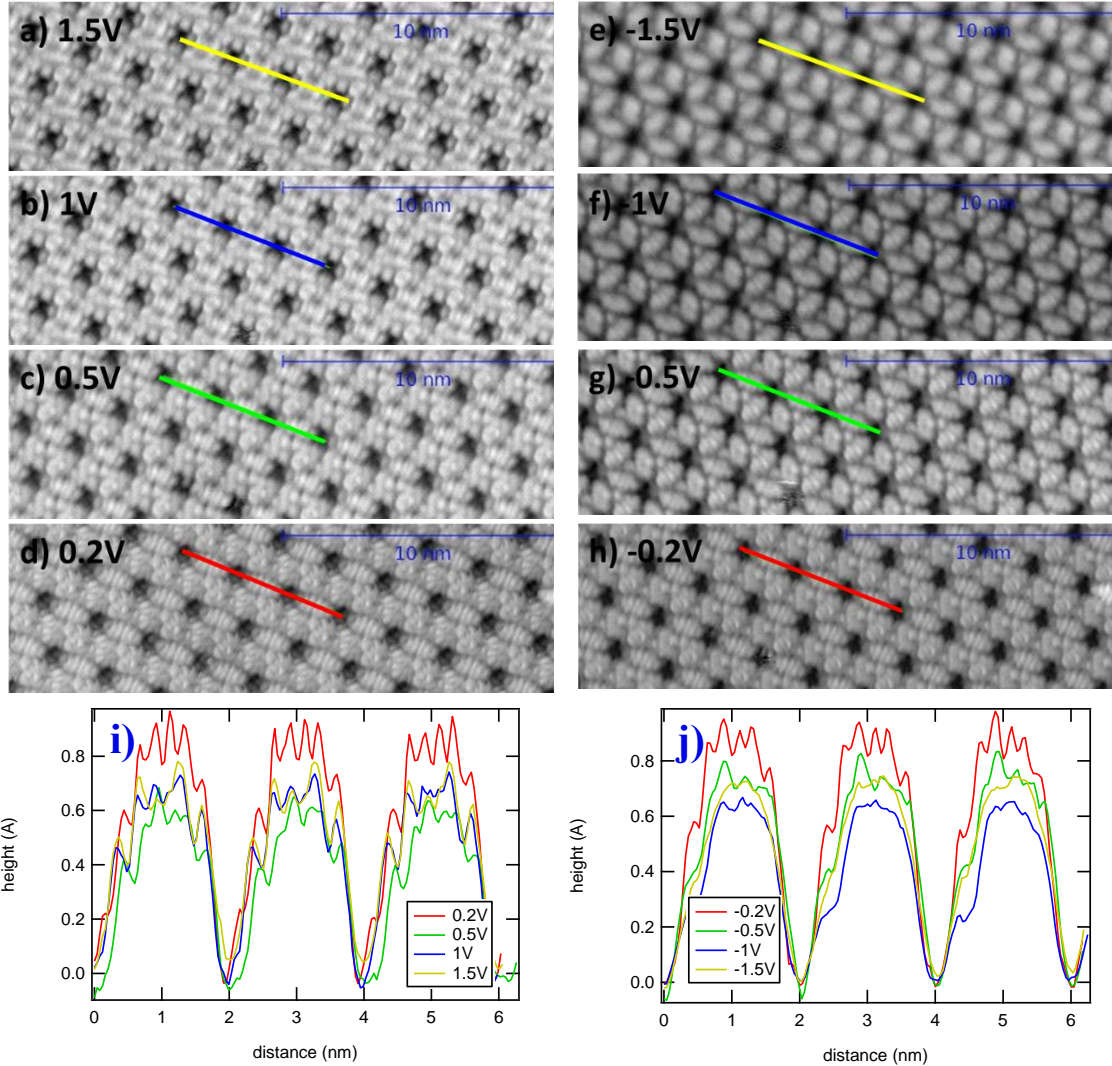


**Figure 8.** Porous network region scanned at different bias voltages. Green lines mark the position used for the height profile. All images size= $20 \times 6 \text{ nm}^2$ . All images were recorded at  $I_t = 300 \text{ pA}$ . Scanning bias voltages: a)  $V_{bias} = 1.5 \text{ V}$ ; b)  $V_{bias} = 1 \text{ V}$ ; c)  $V_{bias} = 0.5 \text{ V}$ ; d)  $V_{bias} = 0.2 \text{ V}$ ; e)  $V_{bias} = -1.5 \text{ V}$ ; f)  $V_{bias} = -1 \text{ V}$ ; g)  $V_{bias} = -0.5 \text{ V}$ ; h)  $V_{bias} = -0.2 \text{ V}$ . i) and j) stack the height profiles of the images above. Colours in images correspond to colours in the lower graphs.

As explained in the introduction, when scanning with STM we are not probing the exact topology of the sample, but its electronic density. Therefore, changing the bias voltage

we can gain access to different molecular orbitals. This is clearly depicted in figure 8a-h that shows the evolution of the molecular orbitals when the same porous network region is scanned while varying the bias voltages. This elegantly proves that the molecular orbitals of molecules are strongly modified when deposited onto metallic surfaces due to their interaction with substrate electrons<sup>14</sup>. Moreover, the Cu coordination atom is hidden for positive voltages, but stands out for negative ones. To get further insight into the orbital character of these networks and its corresponding metal coordination it is necessary to perform scanning tunnelling spectroscopy (STS) and  $dI/dV$  maps, which are planned for forthcoming experiments.

The height profiles extracted at the same position of the above images, show that they are slightly dependent upon the applied voltage. The height is more prominent for lower absolute voltages (0.2V and -0.2V) and decreases for larger absolute values. Spectroscopy and constant height data is necessary to understand the existing relation with the molecular electron density. Table 1 summarises the scanning height obtained from the profiles of Fig.10, which highlights the differences for variable bias voltages.

<b>v (V)</b>	<b>h (Å)</b>	<b>uncertainty (Å)</b>
0.2	0.856	0.006
> 0.2	0.651	0.007
< -0.2	0.690	0.043

**Table 1.** Maxima plateau values of the scanned height for the different ranges of bias voltage. The average value is roughly 0.75 Å.

### 3.1.2 Close packed phase

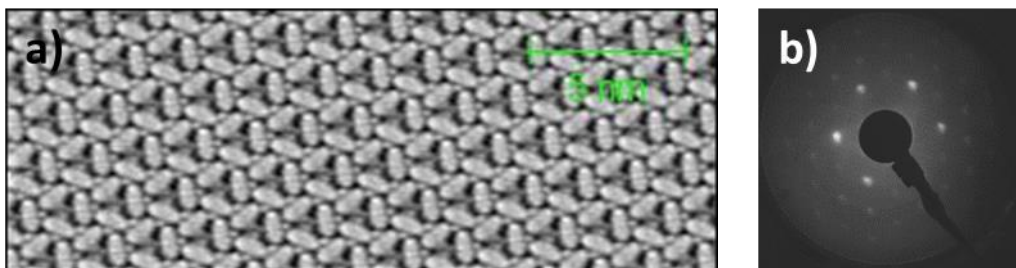


**Figure 9.** Close packed network structure. a) STM image taken at  $I_t = 120\text{pA}$  and  $V_{bias} = 0\text{V}$ . Size =  $100 \times 37\text{nm}^2$ . b) LEED pattern of the compact phase:  $(4\sqrt{3} \times 4\sqrt{3})R30^\circ$  structure. Electron beam energy is 22eV.

The close packed phase, before multilayer formation, occurs whenever higher amounts of molecules than a certain threshold stabilizing the porous phase is evaporated at room temperature and the surface is fully covered by DCA. If the multilayer is present on top of the substrate and subsequently annealed, this phase is observed for lower temperatures than the porous one. As we observe in Figs.9a and Fig. 5, the unit cell of this assembly is smaller than in the porous phase by ~25%. As a consequence, the LEED pattern (Fig.9b) is different too. Here, the structure is a  $(4\sqrt{3}\times 4\sqrt{3})R30^\circ$ , which at 22 eV shares with the porous structure the intense hexagon, but lacks its inner one, so it is  $30^\circ$  rotated with respect to the substrate main spots.

Fig.10 shows a scan of a close packed network changing the bias voltage from negative (bottom) to positive (top). For negative voltages, we observe the molecules assembling into triangles that reminds of the porous network fraction where the Cu adatom coordinates to three DCA molecules. However, in this structure we do not visualize the coordination atom at any voltage value. Given that this phase is a slight modification of the porous one, we believe that Cu adatoms are still embedded in the structure, although we are not able to observe them on STM topography.

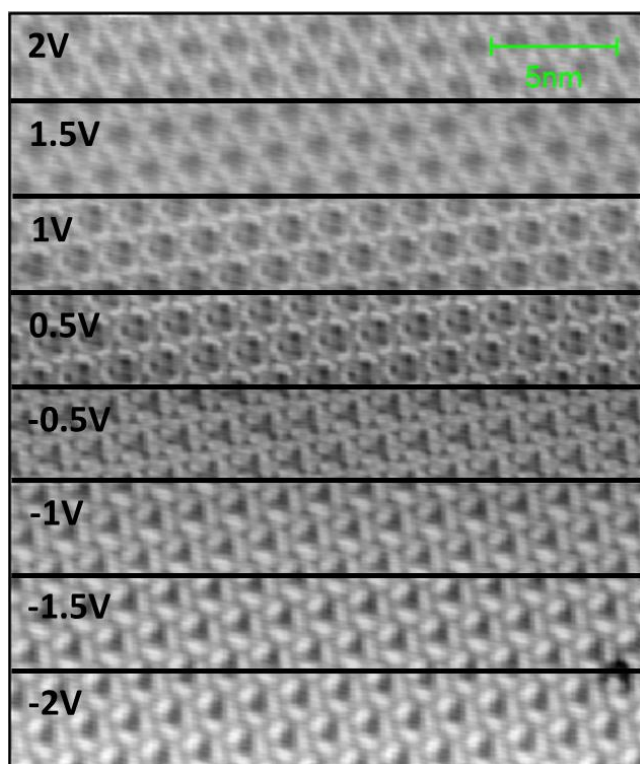


**Figure 10.** STM image of a close packed network as a function of bias voltage. The bias voltage changes as the image is acquired from -2V (bottom) to 2V (top). There is no evidence of any coordination atom at any voltage. Image details:  $I_t=120\text{pA}$ , size= $25\times 30\text{nm}^2$ .

## **3.2. Network modification upon transition metal evaporation**

After achieving extended porous networks, the objective is to investigate the interaction of selected transition metals and study the morphological changes induced on them. Initially, we intended to use the porous network as a nanotemplate for the transition metals (Mn, Co and Fe), i.e., to generate metal clusters (dots) inside each pore of specific size (defined by the cavity dimensions) and have them periodically distributed on the surface (acquiring the periodicity of the network). If this would have worked, we would follow up this work by investigating the magnetic interaction between regularly spaced nanodots. However, these transition elements did not generate the desired clusters within the pores, but resulted in a wide variety of configurations dependent on the element evaporated and sample preparation protocols, which will be discussed in the following.

### **3.2.1 Manganese interaction with DCA networks.**

Manganese evaporated on pristine Cu(111) has been reported to incorporate on the upper terraces of a substrate step, forming a brim alloy<sup>15</sup>. Further deposition of Mn leads to the growth of alloy islands before completely covering the Cu substrate. A subsequent annealing of the system gives rise to more ordered phases as the temperature increases up to 500K.

Such growth conditions are altered when Mn is evaporated at room temperature onto the porous network. We used typically coverages close to 0.25ML of Mn (evaporation time ~10 minutes) as deduced from the island density on pristine Cu(111). Figure 11a shows an overview of the emerging structures, where it is clear that Mn does not preferentially follow the periodicity of the DCA network. The dominant structure consists of large Mn islands of atomic height decorated by disordered molecules. The creation of such amorphous shapes occurs at the expense of the network, which is locally destroyed, as deduced from the surrounding dark regions reminiscent of the bare substrate.

In contrast, some tiny features, brighter than the network, are observed embedded in the porous structure (Figure 11b). These show up at the anthracene molecular backbone, suggesting a local morphological change. In Figure 12 the height profiles of such molecules are studied and show that these molecules appear higher than their neighbours. This suggests that the molecules are lifted at the anthracene edge due to the presence of Mn atoms underneath (note the asymmetric shape of lines 4 and 5 compared to 2 and 3 in Fig. 12 b). Such lifting is feasible given that the DCA backbone is reported to be further

away from the substrate than cyano groups<sup>9</sup>, which would facilitate the incorporation of the Mn under the molecule. We believe that the Mn atoms are quite mobile and diffusing on the surface at room temperature, so that when neighbour molecules are lifted, the network becomes disrupted and the Mn nucleate into large islands.

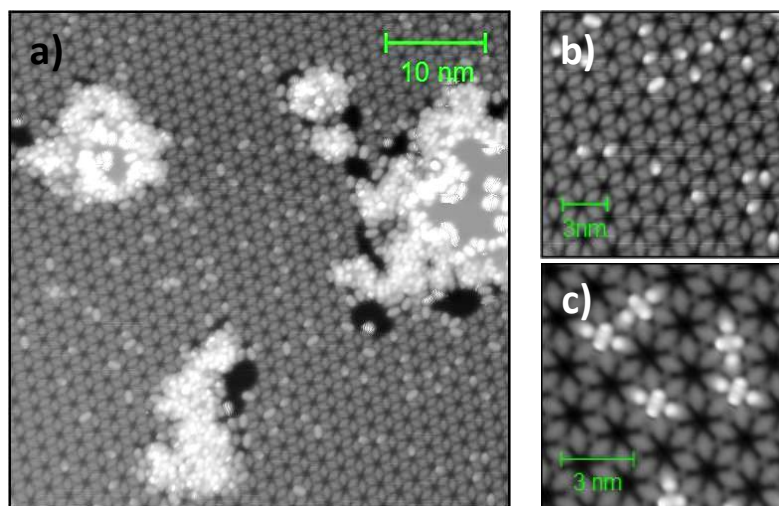


**Figure 11.** *Effect of Mn evaporation upon the porous network. a) Overview image after 0.25 ML of Mn evaporation upon the DCA array. b) Zoom of the porous network showing several bright features located on DCA molecular backbone, resulting from Mn atoms burying themselves underneath (molecules are lifted). c) Some molecules are even found on top of the pores. STM image details: a)  $I_t=1\text{nA}$ ;  $V_{bias}=-1\text{V}$ ,  $size=50\times 50\text{nm}^2$  b)  $I_t=1\text{nA}$ ;  $V_{bias}=-1\text{V}$ ,  $size=15\times 15\text{nm}^2$ . c)  $I_t=100\text{pA}$ ;  $V_{bias}=-0.5\text{V}$ ,  $size=10\times 10\text{nm}^2$ .*

Sometimes, we could find molecules directly on top of a pore (Figure 11c). This is a less probable case that occurs when Mn atoms lift two DCA in opposite sites of the same pore. In this case, the cyano groups of the molecule on the pore centre attach to the backbone tail of the two lifted molecules, or to the two Mn atoms directly underneath.

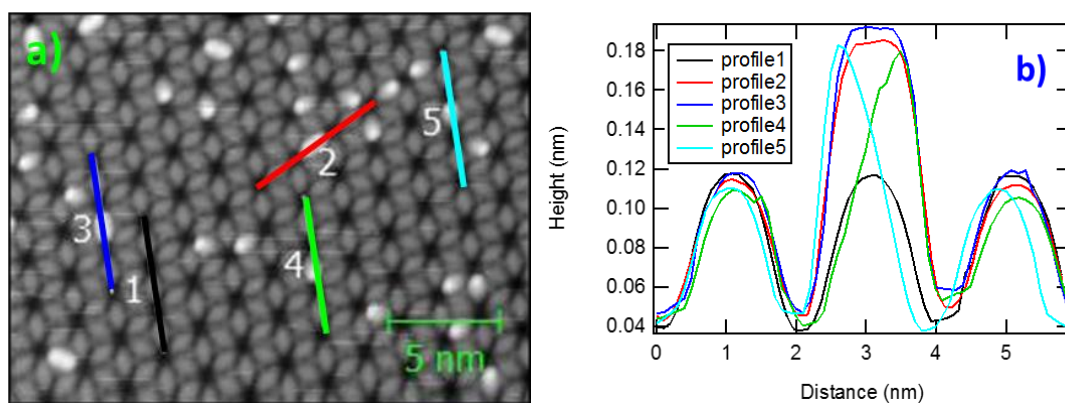


**Figure 12.** Height profiles from bright molecules forming the network after Mn deposition, lifted by the Mn atoms. a) STM image indicating the different height profiles studied in b). Profile 1 is the reference (no lifted molecules); profiles 2 and 3 are lifted by two Mn atoms and profiles 4 and 5 are lifted by a single Mn atom. STM details:  $I_t = 1 \text{ nA}$ ;  $V_{bias} = -1 \text{ V}$ ;  $\text{size} = 22 \times 17 \text{ nm}^2$ . Colours in images correspond to colours in the lower graphs.

### 3.2.2 Cobalt interaction with DCA networks

The evaporation of Co on pristine Cu(111) at room temperature has been reported to lead to the formation of double atomic height triangular islands of Co<sup>16</sup>. Rarely, islands of 1 or 3 layers are observed. The large size of these islands ( $150 \text{ \AA}$ ) denote that Co has a high mobility on Cu(111) at room temperature. Two different triangular orientations appear, which are rotated  $60^\circ$  from each other. Oddly, the magnetization of Co islands has been shown to be strongly reduced upon adsorption of atomic hydrogen due to the hybridization with *d*-orbitals<sup>17</sup>.

The interaction of Co with the DCA networks results in strong modifications of its pristine case. We find that the species deposition order generates different structures. Thus, we prepared samples by depositing Co after DCA network formation (as in Mn) and the reverse procedure, i.e., evaporating Co on the bare Cu and then DCA molecules. We will refer to these systems as *Co/DCA* and *DCA/Co*, respectively. We also used two different molecular coverages: i) *high coverage* (enough to saturate the surface as a carpet,  $t_{\text{dep(DCA)}} = 3'30''$ ), and ii) *low coverage* (just to achieve island formation,  $t_{\text{dep(DCA)}} = 2'$ ). The parameter used to control the molecular coverage was the evaporation time (for a fixed deposition flux). Note that all the evaporations were performed with the substrate kept at room temperature.

The first case of *Co/DCA + low coverage* (formation of a porous network islands and subsequent deposition of Co) are shown in Figure 13. Co is not regularly nanostructured and the integrity of the network is strongly affected. Many defects, non-existing prior to the Co deposition, are now visible, especially near the island clusters and bright features, where the presence of Co is inferred. Height analysis, similar to the one performed for Mn (detailed in Appendix 3), suggests that Co aggregates into islands on the bare Cu that has a single atomic height (close to  $2\text{\AA}$ ). Moreover, the large amount of defects suggests that the destruction of the network occurs because the Co pull out the molecules even more efficiently than the Mn.

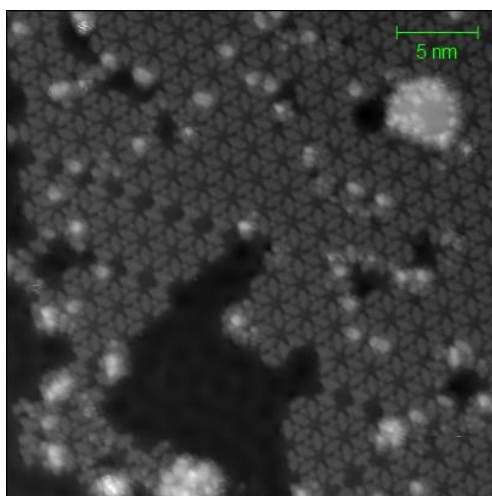


**Figure 13.** *Deposition of Co on molecular network islands: the network is mainly destroyed by the Co presence. STM scan parameters:  $I_t=50\text{pA}$ ;  $V_{bias}=-1\text{V}$ ;  $size=30\times 30\text{nm}^2$ .*

When the DCA coverage is increased in the proximity of the ML and Co is evaporated on top (case of *Co/DCA+ high coverage*) we observe that the porous network is transformed into close packed (see Fig.14). We strongly believe that this is due to the generation of lateral pressure when Co tries to make room for itself to aggregate into islands on top of the Cu substrate. Note that the mobility on the surface of the molecules and atoms is hindered with respect to the previous case so the network cannot be easily shifted laterally and the Co aggregation structures are rather small in size. Note that once again, Co appears to nucleate into mono-atomic height islands ( $\sim 0.2\text{nm}$ ).

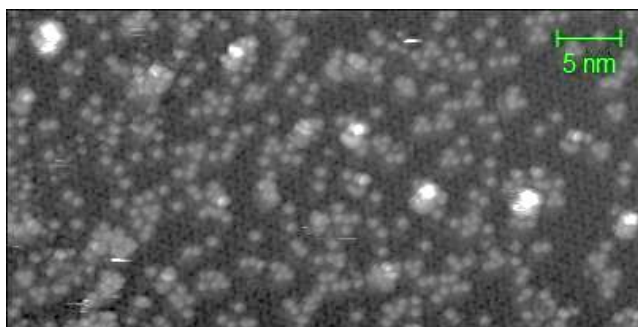


**Figure 14** *Deposition of Co on the extended molecular network results in the conversion of the network into its close packed phase. STM scan parameters:  $I_t=50\text{pA}$ ;  $V_{bias}=-0.2\text{V}$ ;  $size=100\times 50\text{nm}^2$ .*

At this point we reverse the deposition order, evaporating first Co atoms and afterwards the DCA molecules (*DCA/Co*). Figure 15 shows the case for *high coverage* conditions of DCA. As in the previous case, we obtain the compact network. However, now, there is no presence of isolated atoms or small clusters ubiquitous over the network, but larger islands well separated from one another. It must be noted, that these islands are quite often double the atomic height, as expected from under ML deposition of Co on Cu(111).

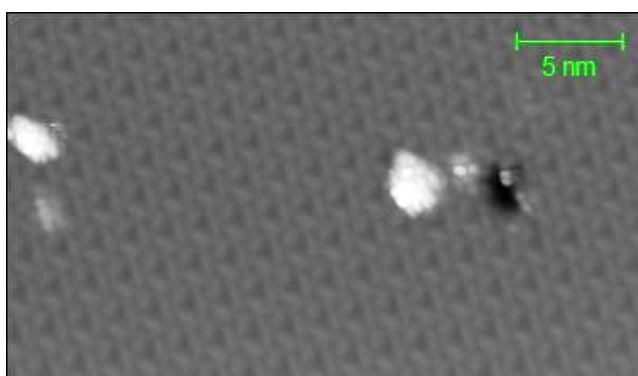


**Figure 15.** *Deposition of DCA on Co with high coverage of DCA leads directly to the formation of the close packed network. STM scan parameters:  $I_t=120\text{pA}$ ;  $V_{bias}=-1\text{V}$ ;  $size=100\times 58\text{nm}^2$ .*

The last case studied is *DCA/Co* with low molecular coverage, so that there are free surface regions. In this case, apart from the expected Co large islands, the molecules ordered into the porous network islands combined with one dimensional chains. Figure 16 shows a close-up of such novel chain structures. We distinguish two coordination possibilities for the chain formation. First, by atom coordination, as clearly observed in the image. This atom cannot be a Cu adatom because it has not been previously observed and we know that it should generate three-fold coordination with DCA. Thus, Co atoms must be responsible for this type of coordination. Second, by molecular cyano bonding. When no atom is observed between two molecules, which coincides with a kink in the chain (highlighted by yellow circles in Figure 16), the molecules appear to be closer to

each other. In this case, there must be a dipole-dipole interaction of the cyano groups of both molecules. Both chain bonding methods have been schematized in Figure 16 b.

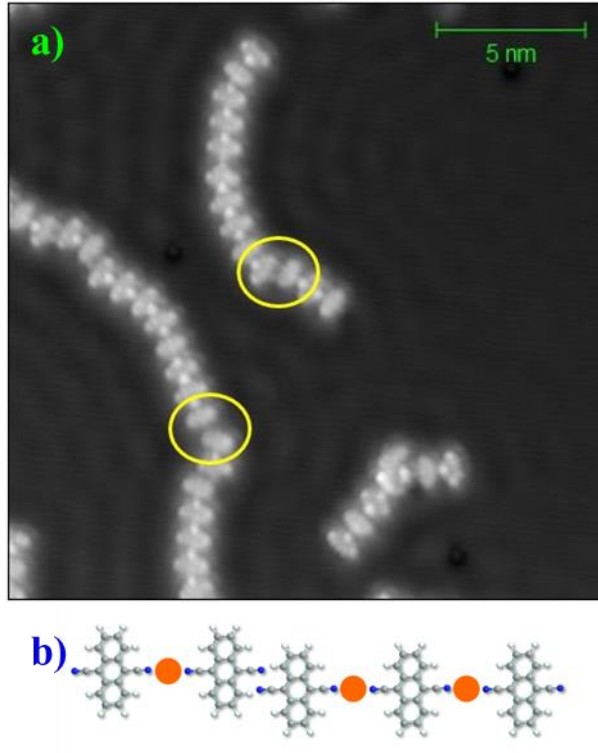


**Figure 16.** The evaporation of some molecules on previously deposited Co, generates one dimensional structures. The DCA chains are coordinated either by Co atoms or by the cyano dipolar interactions (marked by yellow circles). Note the standing waves in the image. Image parameters:  $I_t=120\text{pA}$ ;  $V_{bias}=-0.1\text{V}$ ;  $size=20\times 20\text{nm}^2$ . b) Scheme of the molecular chains and the existing bonding methods. Orange dots correspond to cobalt atoms.

The size (length) and amount of the 1D structures is quite limited compared to the network existing on the surface. This means that the chains are by far less stable than the networks. This leads us to believe that at room temperature chains must be mobile and kinetically active, i.e., continuously forming and breaking up, but we can freeze them by acquiring the images close to liquid He temperatures ( $\sim 5\text{K}$ ).

Table 2 contains a summary of the obtained results for these four sample preparation cases that allows us to shed light upon the interaction of Co with the DCA networks.

	<i>Low coverage</i> ( $t_{\text{evap(DCA)}} = 2'$ )	<i>High coverage</i> ( $t_{\text{evap(DCA)}} = 3'30''$ )
Co/DCA	Destroyed porous network Co clusters in one atomic height	Co turns porous into compact phase Co clusters above one atomic height
DCA/Co	DCA chains and networks Co clusters in one atomic height	DCA forms compact phase networks Co clusters above one atomic height

**Table 2.** Summary of the main results depending upon the preparation conditions (coverage and deposition order).

### 3.2.3 Iron interaction with DCA networks.

Fe is the last transition element that we study in this work seeking to find the resulting assemblies with DCA networks. When we deposit Fe directly on Cu(111) we find that it grows as triangular (sometimes polygonal) islands, as previously reported<sup>18</sup>. Similarly, to Co, the triangular islands grow following the substrate's high symmetry directions, i.e. two different orientations rotated 60° and are generally of double atomic height for low Fe coverages. Figure 17 shows a prototypical Fe island self-assembled in Cu(111), which is studied as a function of bias voltage and current. Note that these images remain practically unchanged, contrary to the molecular networks (Fig. 8 and 10). This is corroborated by height profiles passing through the same position, which yield very similar quantitative values. In particular, the average height is  $\sim 4\text{\AA}$  for this double atomic height island, implying that the atomic height of Fe is close to  $2\text{\AA}$ . The average size of such Fe on Cu islands, extracted from larger images (see Appendix 4), is in average  $150\text{--}200\text{ nm}^2$ . This size will be now compared to the case when Fe is deposited onto the DCA network.

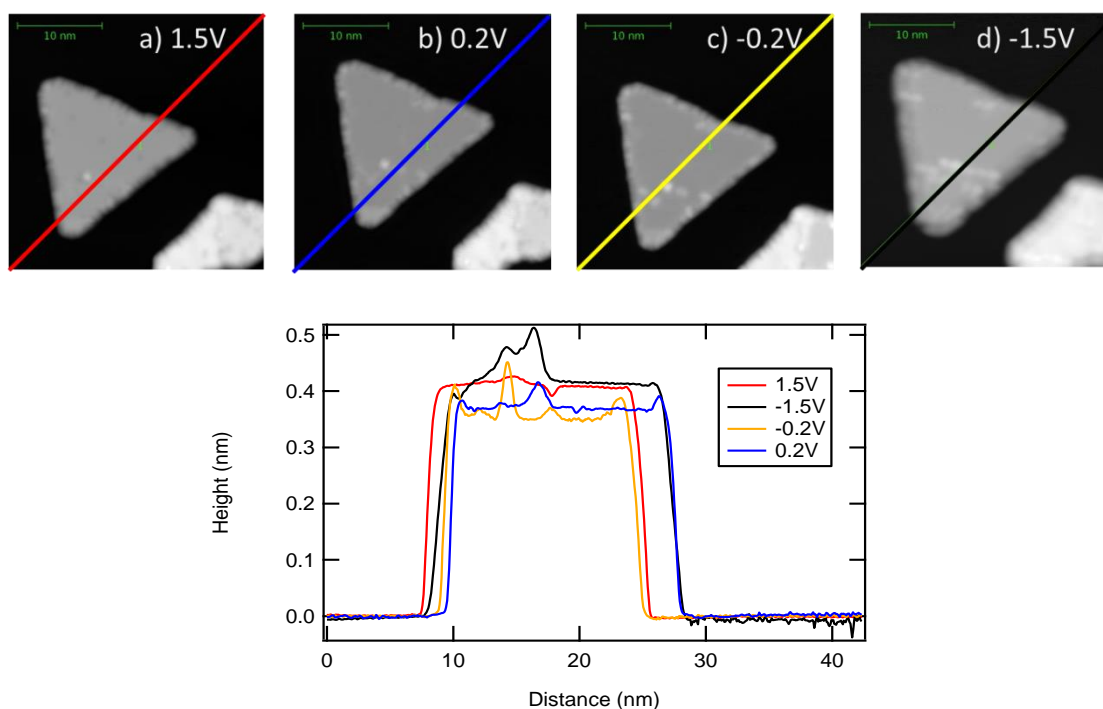


**Figure 17.** Fe island nucleation after deposition of 0.5 ML at room temperature on clean Cu(111). The STM images differ on the bias potential and current parameters used: a)  $I_t = 160\text{ pA}$ ;  $V_{bias} = 1.5\text{ V}$ ; b)  $I_t = 500\text{ pA}$ ;  $V_{bias} = 0.2\text{ V}$ ; c)  $I_t = 500\text{ pA}$ ;  $V_{bias} = -0.2\text{ V}$  d)  $I_t = 160\text{ pA}$ ;  $V_{bias} = -1.5\text{ V}$ . The curves on the lower figure correspond to the height profile lines marked in each image. STM image size =  $30 \times 30\text{ nm}^2$ .

Different samples of Fe on the DCA network have been prepared to study the resulting structures. The quantity of evaporated Fe and the temperature of the substrate during deposition ( $T_{\text{dep}}$ ) has been key parameters when performing this investigation. Once more, the parameter used to control the quantity of Fe is the deposition time ( $t_{\text{dep(Fe)}}$ ) at constant flux.

The first studied case, that will be taken as reference, consists in the evaporation at room temperature of Fe during  $t_{\text{dep(Fe)}}=2'$  (corresponding roughly to 0.1 ML of Fe) on the molecular network. Fig. 18 shows a large overview of such preparation. We observe that the molecular network does have a nanostructuring effect on the Fe, generating dots significantly smaller than the islands when no molecules are present on the clean substrates. Despite the fact that the molecular network is not fully covering the surface (there are wide areas of bare Cu), we observe that Fe is preferentially adsorbed on the molecular islands or at step edges, but not on the clean terraces. As it will be demonstrated, this Fe dot nanostructuring is a general case when DCA molecules are adsorbed on the surface. Note that Fe nanodots on pristine Cu(111) have been reported, but only when the Fe evaporation is done at very low temperatures (12K)<sup>19</sup> or using the buffer layer assisted growth method<sup>20</sup>.

In order to quantify the size and height of these dots, we have extracted the projected area and height of the dots from several STM images, which were afterwards fit to Log-normal and Gaussian functions, respectively, to obtain their most probable values. Note that the obtained maximum heights take as reference the Cu substrate and not the molecules. The resulting distribution of projected areas and height of the dots is plotted in Figure 18 b-c. The calculated central value of the projected area is found to be  $3.04\text{nm}^2$ , which is significantly smaller than the average island size in Fe/Cu(111). These clusters are far larger than single atoms<sup>19</sup>, but smaller than the reported ones using the buffer layer assisted growth method<sup>20</sup>. Regarding the dot height, we find that they are mainly between 0.2nm and 0.5nm, with the most probable value of 0.33nm. This is not a multiple of the Fe atomic height ( $n \cdot 0.2\text{nm}$ ), suggesting that the dot might also have contributions from underlying molecules ( $\sim 0.07\text{nm}$ ). This points towards formation of Fe nanodots on top of the network, but not particularly filling the pores. Note that the maximum height histogram is a truncated Gaussian because the threshold value for a dot height is 0.2nm, which is the monoatomic height.

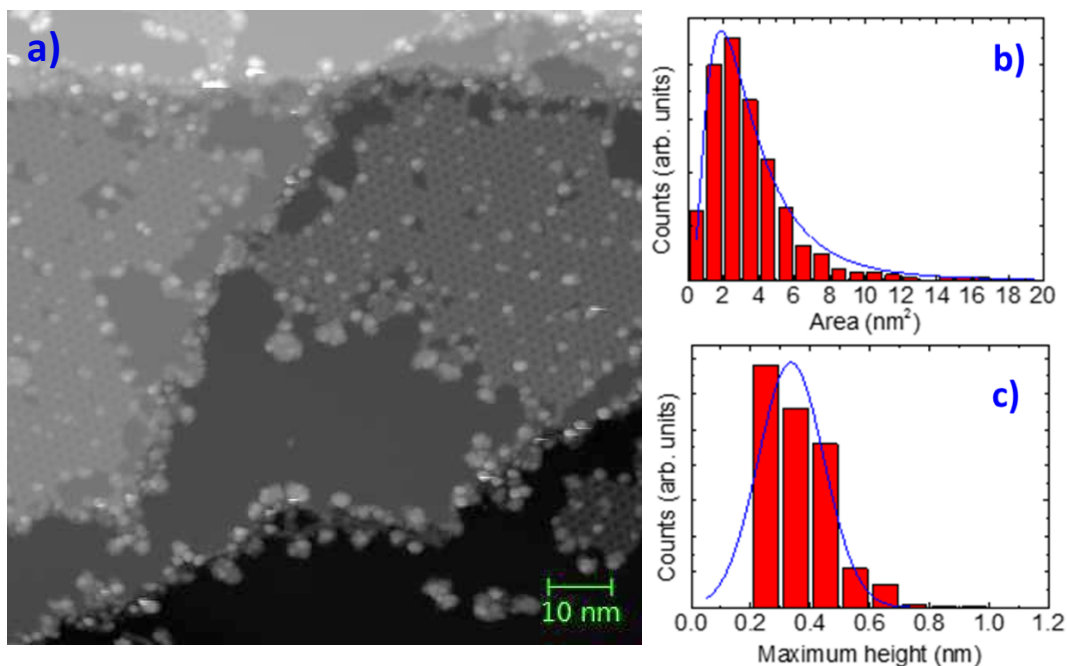


**Figure 18.** Deposition of Fe during 2 minutes (0.1 ML) at room temperature on top of network islands. a) STM image showing the representative assemblies where nanodots are observed as bright protrusions. b) Histogram of the nanodot area found on the DCA islands and fitted to a Lognormal curve in blue. The average area is  $3.04\text{nm}^2$ . c) Histogram of the nanodot height with a Gaussian fitting in blue. The most probable value is 0.33 nm. STM Image parameters:  $I_t = 100\text{pA}$ ;  $V_{bias} = 1.5\text{V}$ ;  $size = 100 \times 100\text{nm}^2$

The following experiment consisted in increasing the quantity of evaporated Fe by increasing the evaporation time to  $t_{\text{dep(Fe)}} = 10'$  (0.5 ML). The resulting assemblies are shown in Figure 19. The image and corresponding histograms indicate that the Fe keeps nucleating as small dots on top of the molecular islands. However, the quantitative analysis shows that these exhibit a slightly larger area centred in  $5.55\text{nm}^2$ , with a broader distribution than for the lower coverage. Simultaneously, these dots become vertically extended since the height histogram is now centred at 0.58nm, which is increased by 0.25 nm with respect to the reference case. This suggests that the dots reach two (or even three) atomic heights and are still on top of the molecular network.

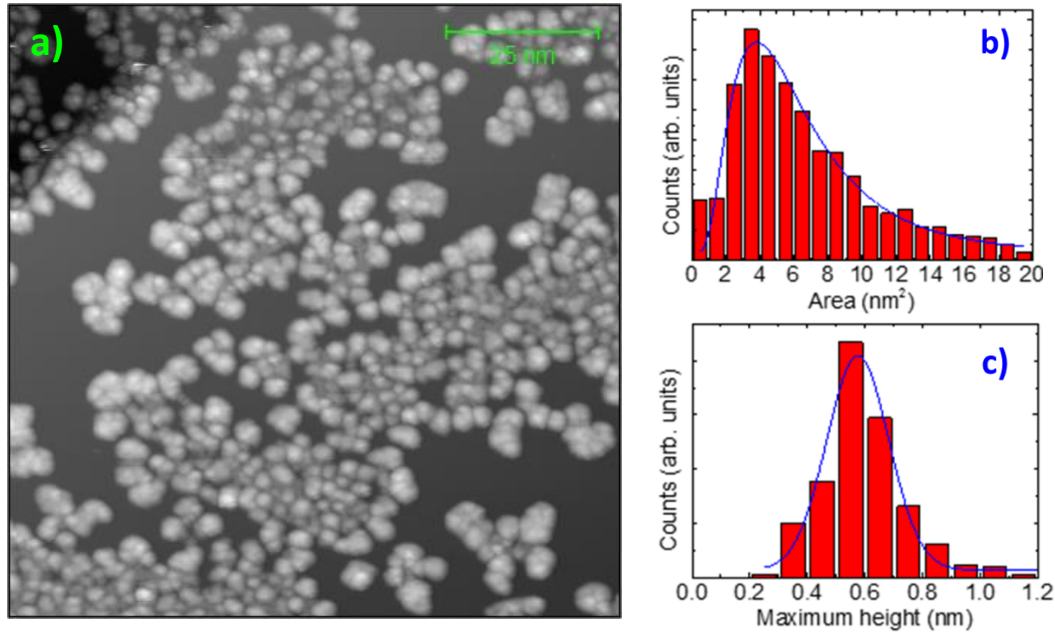


**Figure 19.** Dot structure found after the deposition of a larger quantity of Fe (0.5 ML) at room temperature onto the DCA porous network. a) STM image showing the formation of larger and more extended nanodots than the previous figure. b) Histogram with a Lognormal fitting of the nanodots area, yielding a value of  $5.55\text{nm}^2$ . c) Histogram with Gaussian fitting showing that the most probable dot height is 0.58 nm. STM Image parameters:  $I_t = 100\text{pA}$ ;  $V_{bias} = 1\text{V}$ ; size =  $100 \times 100 \text{nm}^2$ .

Based on the fact that Fe can be nanostructured when deposited at very low temperatures<sup>19,20</sup>, we studied the morphological changes of the dots when Fe is evaporated on the molecular network at lower temperatures ( $T_{\text{dep}} \sim 170\text{K}$ ), but still far from 12K. In this case, we start with a low Fe coverage (0.15 ML) close to the first reference preparation. Figure 20 shows the resulting structures after this low temperature deposition. It is clear that the Fe dots are sharper than when depositing at room temperature and the quantitative analysis of the area histogram shows that the most probable value is  $1.85\text{nm}^2$ , significantly smaller than before. Regarding the dot height, the histogram is now centred in 0.28nm, suggesting that most of the dots are on top of the network and exhibit single atomic height. This result suggests that the mobility of Fe is strongly affected by both the temperature and the presence of the DCA network. Thus, an easy way to control the resulting nanodot size is to simply vary the temperature while evaporating the Fe.

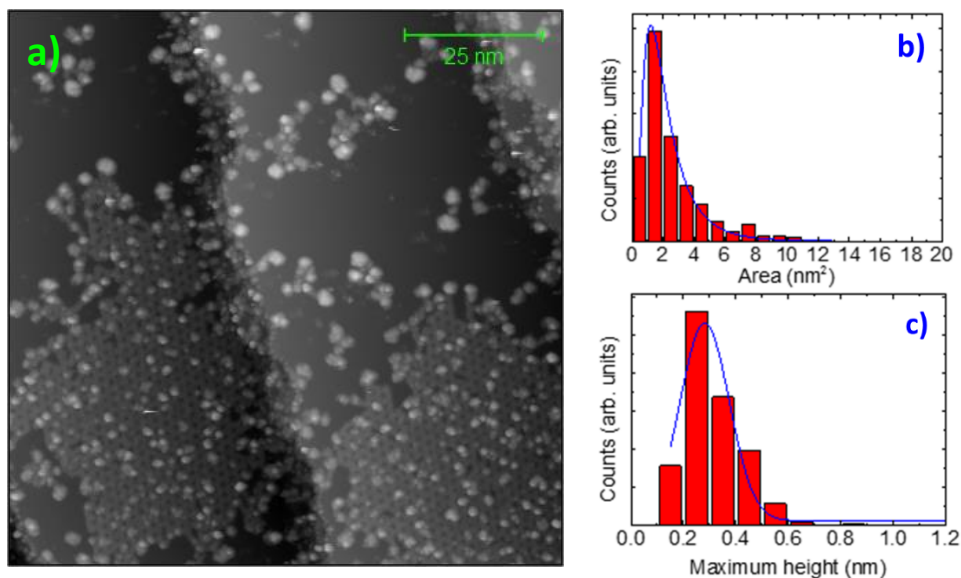


**Figure 20.** Dot structure found after low coverage (0.15 ML) deposition of Fe at low temperature ( $T_{dep} \approx 170K$ ) on the molecular network. a) STM image showing the formation of the sharpest nanodots. b) Histogram with a Lognormal function fit of the dot area, providing a value of  $1.85 \text{ nm}^2$ . c) Histogram including a Gaussian fit showing that the average dot height is  $0.28 \text{ nm}$  (an Fe atomic height and DCA molecule). STM Image parameters:  $I_t = 40 \text{ pA}$ ;  $V_{bias} = 1.5 \text{ V}$ ;  $\text{size} = 100 \times 100 \text{ nm}^2$ .

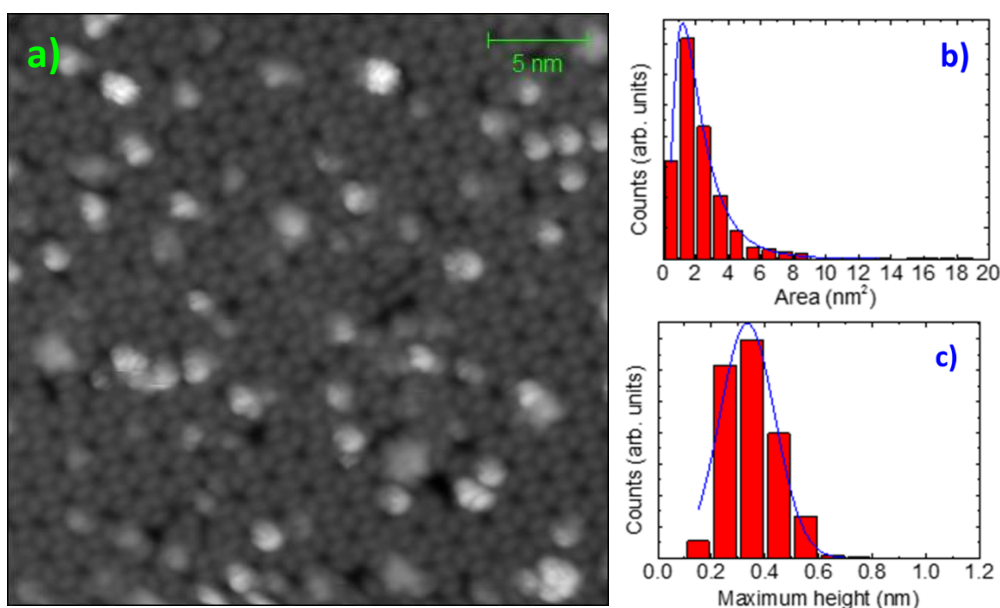


**Figure 21.** Dot structure found after low coverage (0.15 ML) deposition of Fe at low temperature ( $T_{dep} \approx 170K$ ) on the molecular network. with a subsequent annealing at RT during 15 minutes. a) STM image showing the existence of sharp nanodots. b) Histogram with a Lognormal function fit of the dot area, providing a value of  $1.86 \text{ nm}^2$ . c) Histogram including a Gaussian fit showing that the average dot height is  $0.33 \text{ nm}$ . STM Image parameters:  $I_t = 40 \text{ pA}$ ;  $V_{bias} = -1.5 \text{ V}$ ;  $\text{size} = 30 \times 30 \text{ nm}^2$ .

The remaining question is if these sharp nanodots are still stable when the sample is warmed up. For this purpose, we studied the stability of the dots when we post-anneal the substrate to room temperature after its low temperature deposition. Figure 21 shows the resulting dot arrays which have been quantitatively analysed as the previous cases. We find that the dots are highly stable, as we find almost no increase in area or height of the dots or a significant destruction of the network. In particular, the area distribution is practically as sharp, with a central value of  $1.86\text{nm}^2$  and the height histogram (centred in  $0.33\text{nm}$ ) only increase slightly (by  $0.05\text{ nm}$ ) with respect to the non-annealed case.

As a summary of the Fe deposition experiments onto the DCA network, Table 3 shows the average value of the nanodot height and its average area for each of the described experiments. It highlights that we can control de nanodot size by both the quantity deposited as well as by the deposition temperature. Significantly, the reduced mobility of Fe when the DCA network is present allows us to deposit Fe below room temperature and get practically unaffected grains when the sample is post-annealed to room temperature.

$t_{\text{dep}}$ (min)	$T_{\text{dep}}$ (K)	Post-Anneal	Average height (nm)	Area ( $\text{nm}^2$ )
2 (0.10 ML)	RT	no	$0.33 \pm 0.02$	$3.04 \pm 0.10$
10 (0.5 ML)	RT	no	$0.57 \pm 0.02$	$5.55 \pm 0.19$
2 (0.15 ML)	170	no	$0.28 \pm 0.01$	$1.85 \pm 0.04$
2 (0.15 ML)	170	RT	$0.33 \pm 0.01$	$1.86 \pm 0.02$

**Table 3.** *Fe nanodots average height and Area central values obtained from the quantitative analysis of the histograms obtained from the STM images and fitted with Gaussian and Lognormal functions, respectively. The results indicate the values obtained for the discussed cases.*

## 4. CONCLUSIONS

We have achieved extended metal-organic molecular networks by self-assembly of DCA molecules on a Cu(111) substrate. We demonstrated that the formation of two different phases (the porous one and the close packed one) depends on the amount of molecules on the first layer. In both cases we find that there is a strong dependence of the imaging modes on the applied voltage.

Once the network was well characterized, we chose to deposit three different transition metals (Mn, Fe and Co) making use of the nanotemplating from the porous network. However, we did not observe preferential growth of metal clusters (dots) inside the pores, but quite different behaviours depending on the element used.

The evaporation of Mn on the DCA porous network shows that Mn has a tendency to squeeze underneath the molecules and aggregate into large islands. We infer that the mechanism consists in lifting up single molecules and then diffusing to reach the islands. The Mn islands exhibit molecules accumulated randomly on their top, but leave the rest of the network practically undisturbed.

The interaction of Co with the porous network shows a similar behaviour to Mn in terms of nucleating islands. In this case, the Co disrupts more efficiently the DCA networks displacing laterally the DCA molecules. In consequence, they generate significant lateral pressure capable of transforming an extended porous network into a close packed one. Depending on the preparation procedure we found one-dimensional structures (chains) coordinated by Co or via dipole-dipole interaction.

Fe has been the only element generating regular nanodots. However, the dots did not nucleate inside the pores but on top of the molecules or Cu coordinating atoms. We have been able to control the grain size on the porous network by changing two different parameters: The Fe coverage and the deposition temperature,  $T_{\text{dep}}$ . In particular, increasing the Fe quantity results in an increase of the grain size and widens the distribution. On the other hand, reducing the deposition temperature reduces the size nanodots overall volume, finding it to be stable after warming the sample up to room temperature.

As outlook we would like to study the electronic structure of both networks, by acquiring  $dI/dV$  maps. In this way we will determine the molecular orbitals and the coordination to

the metal atoms. This is particularly important for the close packed phase where the presence of Cu adatoms is not clear.

Aside from this, we plan to investigate the magnetic signal of the Fe nanodots. For this purpose, we wrote proposals for XMCD beamlines to study the dependence of the magnetic signal to the cluster volume.

## 5. BIBLIOGRAPHY

1. Binnig, G. *et al.* Tunneling through a controllable vacuum gap. *Applied Physics Letters*. **40**, 178–180 (1982).
2. Binnig, G. & Rohrer, H. Scanning microscopy- from birth to adolescence. *Reviews of modern physics*. **59**, 165 (1987).
3. Drakova, D. Theoretical modelling of scanning tunnelling microscopy, scanning tunnelling spectroscopy and atomic force microscopy. *Rep. Prog. Phys.* **64**, 205–290 (2001).
4. Cohen-Tannoudji, C. Quantum mechanics. *John Wiley & Sons*. (1977).
5. Lafayette, W. Physical review letters. *Phys. Rev. Lett.* **57**, 8–11 (1986).
6. Krull, C. Electronic structure of metal phthalocyanines on Ag(100). PhD (2012).
7. Wintjes, N. Tailoring Supramolecular Assemblies on a Metal Surface by Specifically Functionalized Porphyrins. PhD (2007).
8. Tersoff, J. & Hamann, D.R. Theory and Application for the Scanning Tunneling Microscope. *Phys. Rev. Lett.* **50**, 1998–2001 (1983).
9. Pawin, G. *et al.* A Surface Coordination Network Based on Substrate-Derived Metal Adatoms with Local Charge Excess. *Angewandte Chemie International Edition*. **47**, 8442–8445 (2008).
10. Zhang, J. *et al.* Probing the spatial and momentum distribution of confined surface states in a metal coordination network. *Chem. Commun. (Camb)*. **50**, 89–92 (2014).
11. Barth, J. V. Molecular Architectonic on Metal Surfaces. *Annu. Rev. Phys. Chem.* **58**, 375-407 (2007).
12. Lingenfelder, M. A. *et al.* Towards Surface-Supported Supramolecular Architectures : Tailored Coordination Assembly of 1,4-Benzenedicarboxylate and Fe on Cu(100). *Chemistry-A European Journal*. **10**, 1913-1919. (2004)
13. Faraggi, M. N. *et al.* Bonding and Charge Transfer in Metal – Organic Coordination Networks on Au(111) with Strong Acceptor Molecules. *The*

- Journal of Physical Chemistry C.* **116**, 24558-24565 (2012).
14. Repp, J., Meyer, G., Joachim, C. & Stojkovic, S. M. Molecules on Insulating Films : Scanning-Tunneling Microscopy Imaging of Individual Molecular Orbitals. *Phys. Rev. Lett.* **94**, 026803 (2005).
  15. Schneider, J., Rosenhahn, A. & Wandelt, K. STM measurements on alloy formation during submonolayer growth of Mn on Cu(111). *Applied surface science.* **142**, 68-74 (1999).
  16. De la Figuera, J., et al. Scanning-tunneling-microscopy study of the growth of cobalt on Cu(111). *Phys. Rev. B.* **47** 13043 (1993).
  17. Park, J., Park, C., Yoon, M. & Li, A. Surface Magnetism of Cobalt Nanoislands Controlled by Atomic Hydrogen. *Nano letters.* **17**, 292-298 (2017).
  18. Shen, J., Pierce, J. P., Plummer, E. W. & Kirschner, J. The effect of spatial confinement on magnetism : films , stripes and dots of Fe on Cu(111). *Journal of Physics: Condensed Matter.* **15**, 1–30 (2002).
  19. Negulyaev, N. N. *et al.* Effect of strain relaxations on heteroepitaxial metal-on-metal island nucleation and superlattice formation : Fe on Cu(111). *Phys. Rev. B.* **79**, 195411 (2009).
  20. Pierce, J. P. et al. Ferromagnetic Stability in Fe Nanodot Assemblies on Cu(111) Induced by Indirect Coupling through the Substrate. *Phys. Rev. Lett.* **92**, 237201 (2004).
  21. Marder, M. P. Condensed matter physics. *John Wiley & Sons.* (2000).
  22. Gulde, M. Development of an Ultrafast Low-Energy Electron Diffraction Setup. PhD (2015).
  23. Schirone, S. Scattering di elettroni in sistemi bidimensionali con forte accoppiamento Spin-Orbita. PhD (2012).